



# Geometric distortions in FMCW SAR images due to inaccurate knowledge of electronic radar parameters: analysis and correction by means of corner reflectors

C. Esposito<sup>a</sup>, A. Natale<sup>a</sup>, G. Palmese<sup>b</sup>, P. Berardino<sup>a</sup>, S. Perna<sup>a,c,\*</sup>

<sup>a</sup> Institute for Electromagnetic Sensing of the Environment (IREA), National Research Council of Italy (CNR), Napoli, Italy

<sup>b</sup> Elettra Microwave S.r.l., Napoli, Italy

<sup>c</sup> Department of Engineering (DI), Università degli Studi di Napoli "Parthenope", Napoli, Italy

## ARTICLE INFO

### Keywords:

Synthetic Aperture Radar (SAR)  
FMCW SAR  
Airborne SAR  
Corner Reflectors  
Radar parameter estimation

## ABSTRACT

In the last years the Frequency Modulated Continuous Wave (FMCW) technology has been playing an ever greater role in the realization of compact, light and cheap Synthetic Aperture Radar (SAR) systems to be mounted onboard small, low altitude platforms such as airplanes, helicopters and drones.

To correctly focus FMCW SAR images, it is necessary to accurately know some system parameters, including the frequency sweep rate of the signal transmitted by the radar. It may happen, however, that this frequency sweep rate is not very accurately measured by the radar provider, and thus an incorrect value of this parameter is used during the SAR data focusing procedure. This may produce serious geometric distortion effects in the focused FMCW SAR images. To circumvent these problems, in this work we present a procedure that estimates the frequency sweep rate actually employed by the FMCW radar, thus providing a key information that can be then profitably used to achieve the correct focusing of the SAR data acquired by the radar system at hand. More specifically, we propose an algorithm that exploits on one side the focused SAR images corrupted by the geometric distortion effects induced by the inaccurate knowledge of this radar parameter, and on the other side the very precise in-situ measurements of the positions of a limited number of Corner Reflectors (CRs) properly deployed over the observed scene.

The effectiveness of the proposed algorithm has been tested on real data acquired by an airborne X-band FMCW SAR system.

## 1. Introduction

Synthetic Aperture Radar (SAR) systems (Franceschetti and Lanari, 1999; Moreira et al., 2013) are microwave remote sensing instruments that are mounted onboard moving platforms, such as satellites (Buckreuss et al., 2009; Franceschetti and Lanari, 1999; Moreira et al., 2013; Torres et al., 2012; Venturini et al., 2008) (spaceborne systems) ground track rails (Tarchi et al., 2003) (ground-based systems), airplanes (Hensley et al., 2001; Horn et al., 2009; Meta et al., 2012; Perna et al., 2016; Pinheiro et al., 2018; Rombach et al., 2003; Ruault du Plessis et al., 2011), helicopters (Perna et al., 2019) and more recently drones (Lort et al., 2018; Aguasca et al., 2013) (aerial systems).

Spaceborne SAR systems present the very attractive feature of ensuring coverage of very wide areas, thus enabling an almost global monitoring of the Earth's surface. On the other side, compared to the spaceborne systems, the aerial ones guarantee a much higher

operational flexibility. Indeed, they allow to timely reach the area of interest, to fly practically along any direction, and to keep very short the so called revisiting time, that is, the time interval elapsing between subsequent observations of the same area. For these reasons, aerial SAR systems are particularly sound for disasters and crisis management, and represent a monitoring solution somehow complementary to that guaranteed today by the existing Earth observation spaceborne SAR infrastructures. In this framework, the technological development of SAR systems seems to be dictated in the last years by two contrasting trends. On one side, the development of spaceborne SAR systems (Torres et al., 2012) aimed at illuminating larger and larger areas, through the exploitation of advanced acquisition modes, such as the ScanSAR (Franceschetti and Lanari, 1999; Gebert et al., 2010; Moreira et al., 2013; Tomiyasu, 1981) or the TOPS (De Zan and Monti Guarnieri, 2006; Gebert et al., 2010; Moreira et al., 2013) ones, which allow to significantly enlarge the across-track coverage guaranteed by the

\* Corresponding author at: Department of Engineering (DI), Università degli Studi di Napoli "Parthenope", Napoli, Italy.  
E-mail address: [perna@uniparthenope.it](mailto:perna@uniparthenope.it) (S. Perna).

conventional Stripmap acquisition mode (Franceschetti and Lanari, 1999; Moreira et al., 2013). On the other side, the development of SAR systems to be mounted on aerial platforms smaller and smaller, aimed at guaranteeing fast and flexible monitoring, possibly at high resolution, of confined areas.

With reference to the design of the latter class of SAR systems, reduction of their size and weight (and, when possible, of the corresponding realization costs) has become therefore a technological paradigm that has been followed in the last years, also due to the amazing growth of the technologies related to the realization of very small and light aerial platforms, such as Unmanned Aerial Vehicles (UAVs) and drones. In this regard, the Frequency-Modulated Continuous-Wave (FMCW) technology (Richards et al., 2010; Meta et al., 2007) is gaining increasing interest as a valid alternative to the more conventional pulse one. Indeed, unlike the pulse radar systems, which require high peak transmission power, FMCW systems operate with constant low transmission power. In addition, the operating principle of FMCW SAR systems makes it possible to keep the sampling frequency of the analog to digital converter significantly smaller than the bandwidth of the transmitted signal. On the other hand, the operating principle of the FMCW SAR limits the maximum distance of interest to a few kilometers, which is of course an insurmountable constraint for spaceborne systems, whereas it is safely acceptable for the acquisition geometry of several aerial platforms, especially for the small-size ones, which typically flight at very low altitudes. Summing up, FMCW SAR systems are particularly tailored to small aerial platforms, since their architecture complexity, which is lower than that of the pulse SAR systems, involves a reduction of size, weight and realization costs.

Turning to the problems related to the SAR data focusing process, which is necessary to obtain high resolution images and products (Franceschetti and Lanari, 1999) starting from the radar data recorded onboard (typically named raw data), we note that this procedure is quite similar for FMCW or pulse systems. More specifically, once the SAR raw data are focused along the *range* (i.e., across-track) direction (Franceschetti and Lanari, 1999), the subsequent processing steps aimed at focusing the SAR data also in the *azimuth* (i.e., along-track) direction (Franceschetti and Lanari, 1999) are practically the same in the two cases, provided that the stop-and-go approximation can be assumed valid, as it always happens if the adopted Pulse Repetition Frequency (PRF) is well higher than the Doppler bandwidth of the system (Meta et al., 2007). In other words, the overall data processing chain to be adopted to focus FMCW or pulse SAR data differs only for the very beginning step, namely, the range focusing procedure. In particular, in the FMCW case, this processing step basically consists in the computation of a Fourier transform followed by the application of a linear mapping that allows coding the domain of the frequencies of the recorded data into the domain of the radar-to-target distances, with a resolution proportional to the inverse of the bandwidth of the transmitted signal (Richards et al., 2010). In this regard, it is worth underlining that to correctly build the above mentioned mapping rule, it is necessary that the nonlinearities of the frequency of the signal recorded onboard are negligible (Meta et al., 2007), and that the electronic parameters of the radar are perfectly known. When these two conditions are not satisfied, geometric as well as radiometric aberrations are expected in the final focused image. More specifically, if the frequency sweep rate of the signal transmitted by the FMCW radar is not stable (that is, not constant) over the transmission time, differences between the nonlinearities of the transmitted signal and the corresponding received echoes may occur (Meta et al., 2007). To compensate for the effects induced by these nonlinearities, a proper estimation procedure has been proposed in (Meta et al., 2007).

On the other side, even assuming that the frequency sweep rate of the FMCW signal is constant, it is possible that the value of this radar parameter is not very accurately measured by the radar supplier. In this work, we address the problems arising in the latter case. In particular,

we show that use of an erroneous value of this radar parameter during the focusing procedure may seriously impair the quality of the final SAR images, producing an undesired stretch of the image along the range direction. To compensate for this geometric effect, we propose a procedure aimed at estimating the frequency sweep rate actually employed by the radar. The proposed algorithm exploits on one side the SAR image obtained by using during the range focusing step the erroneous frequency sweep rate provided by the radar supplier. On the other side, the algorithm exploits the in-situ measurements, carried out through accurate Differential Global Positioning System (D-GPS) techniques, of the positions of a limited number of Corner Reflectors (CRs) properly deployed over the illuminated area.

The estimation procedure is based on a Least Square (LS) approach that provides, in addition to the estimate of the searched frequency sweep rate actually employed by the radar, also the estimate of the internal uncompensated time delay that may be present in the radar electronics introducing an erroneous rigid range shift of the final SAR image.

It is stressed that the presented algorithm requires to execute the overall SAR focusing procedure at least twice: first, by using the available frequency sweep rate value provided by the radar supplier, after, by accounting for the achieved estimates. On the other side, it is worth stressing that for a generic FMCW SAR system the proposed estimation procedure must be applied only once, since the estimated radar parameters can be profitably used to focus the data acquired by the system during other campaigns and missions. It is also noted that the implementation of the proposed procedure comes at zero cost, since the deployment of a number of CRs over the area to be illuminated is a standard operating procedure for the calibration of newborne SAR systems (Wimmer et al., 2000).

The algorithm has been tested on real data acquired by an airborne X-band FMCW SAR system.

This paper is organized as follows. In Section 2, we discuss the distortion effects induced on the focused FMCW SAR images when an uncompensated time delay is present in the radar electronics or/and when an erroneous value of the frequency sweep rate is used during the focusing procedure. The proposed estimation approach is described in Section 3. Section 4 shows the experimental results. Section 5 is dedicated to some concluding remarks.

## 2. Problem statement

The FMCW SAR differs from the pulse one in that the electromagnetic signal is continuously transmitted by the radar (hence the name Frequency Modulated Continuous Wave). To show the operating principle of a FMCW SAR let us refer to Fig. 1 and assume that the condition ensuring the stop-and-go approximation is satisfied (Meta et al., 2007). Let  $s_{rx}(\cdot)$  be the signal transmitted by the radar at a generic fixed azimuth coordinate (that is, at a generic fixed slow time); its expression is:

$$s_{rx}(t) = \exp\left(j2\pi\left(f_c t + \frac{1}{2}\alpha t^2\right)\right), \quad (1)$$

where  $f_c$  is the carrier frequency,  $t$  the fast time and  $\alpha$  the frequency sweep rate, which is equal to the ratio between the bandwidth  $B$  of the transmitted signal and the transmission window  $T$  (Richards et al., 2010). According to (1), the instantaneous frequency, say  $f_r$ , of the transmitted signal changes over time as follows:

$$f_r(t) = f_c + \alpha t. \quad (2)$$

Let us consider a generic target placed at a distance  $R$  from the phase center of the radar antenna (IEEE Standard Definitions of Terms for Antennas, 1983, Teichman, 1973): it produces an echo  $s_{rx}(\cdot)$  that is received by the radar while  $s_{tx}(\cdot)$  is still being transmitted (see again Fig. 1). More specifically,  $s_{rx}(\cdot)$  is a delayed version of  $s_{tx}(\cdot)$ , and its

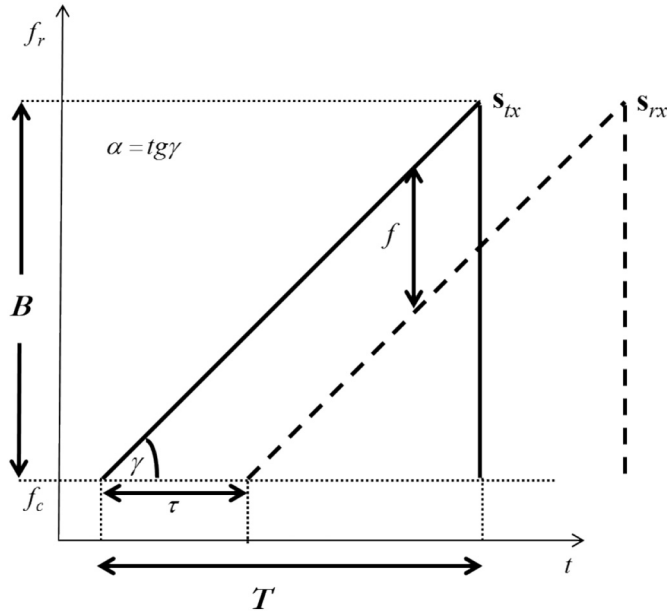


Fig. 1. Operating principle of a FMCW SAR.

expression is:

$$s_{rx}(t) = \exp\left(j2\pi\left(f_c(t - \tau) + \frac{1}{2}\alpha(t - \tau)^2\right)\right), \quad (3)$$

where

$$\tau = 2R/c \quad (4)$$

is the so called round-trip time. Note that in (3) the constant complex weight due to the target reflectivity, as well as the attenuation factor due to the propagation path have been neglected for the sake of simplicity, since they are inessential for our scopes.

Unlike the pulse radar, the FMCW one does not measure the radar-to-target distance  $R$  directly from the received signal  $s_{rx}(\cdot)$  in (3), but instead from a signal, say  $s_{IF}(\cdot)$ , obtained by mixing the received signal  $s_{rx}(\cdot)$  in (3) and the transmitted signal  $s_{tx}(\cdot)$  in (1), and subsequently applying a low-pass filtering. The expression of  $s_{IF}(\cdot)$  is:

$$s_{IF}(t) = \exp\left(j2\pi\left(ft + f_c\tau - \frac{1}{2}\alpha\tau^2\right)\right), \quad (5)$$

where  $f$  is the so called beat frequency (Meta et al., 2007), which is proportional to the round-trip time:

$$f = \alpha\tau = \frac{2\alpha R}{c}, \quad (6)$$

as can be easily derived from the expressions of the beating signals in (1) and (3). Note that use of (4) has been done in the last equality of (6). It is also noted that all the three terms in (5) depend on the radar-to-target distance  $R$ . In particular, the term  $ft$ , which depends on  $R$  through  $f$ , see (6), depends on the fast time  $t$  as well. The two terms  $f_c\tau$  and  $\alpha\tau^2/2$ , which depend on  $R$  through  $\tau$ , see (4), are instead both independent of the fast time  $t$ . In the following, we concentrate on the  $t$ -dependent term, which determines the range location (Franceschetti and Lanari, 1999; Meta et al., 2007), within the focused SAR image, of the pixel relevant to the considered target. In this regard, we note that inverting Eq. (6) we obtain the following linear mapping rule:

$$R = \frac{cf}{2\alpha} \quad (7)$$

which relates the radar-to-target distance  $R$  and the beat frequency  $f$  of the signal  $s_{IF}(\cdot)$  in (5). Based on this consideration, the range focusing step (Franceschetti and Lanari, 1999) of FMCW SAR raw data consists

in calculating the spectrum of the signal  $s_{IF}(\cdot)$  and subsequently converting the spectral variable  $f$  into the variable  $R$  according to the mapping rule in (7) (Meta et al., 2007). This allows locating along the range direction of the SAR image (with a resolution proportional to  $1/B$ ) the pixel relevant to a generic target according to its distance from the radar, provided that the relation in (4) is rigorously valid and the electronic parameter  $\alpha$  in (7) is accurately known. Unfortunately, in real radar systems, both these two conditions may be not satisfied. Indeed, the presence of unknown propagation delays in the radar electronics may produce an unknown time misalignment between the transmitted signal  $s_{tx}(\cdot)$  and the received signal  $s_{rx}(\cdot)$ , thus modifying the relation in (4), and therefore the mapping rule in (7). Moreover, even assuming that nonlinearity effects do not occur when transmitting the signal in (1) (Meta et al., 2007), it may happen that the (constant) frequency sweep rate  $\alpha$  in (6) is not very accurately measured by the radar supplier, thus inducing an error when building the mapping rule in (7). The presence of such error sources, which is quite common in real radar systems, may impair the geometrical accuracy of the final SAR image, mainly inducing target location shifts. To better clarify this point, we first address separately the effects of such error sources, and then we analyze them jointly.

Let us first suppose that the frequency sweep rate  $\alpha$  is known with infinite accuracy, but an unknown and constant propagation delay, say  $\mu$ , in the radar electronics exists. This modifies the expression of the round-trip time measured by the radar (say  $\tilde{\tau}$ ) as follows:

$$\tilde{\tau} = \tau + \mu, \quad (8)$$

where  $\tau$  is the ideal round-trip time related to the true radar-to-target distance. According to (8), the beat frequency (say  $\tilde{f}$ ) of the signal  $s_{IF}(\cdot)$  is modified as follows:

$$\tilde{f} = \alpha\tilde{\tau} = \frac{\alpha 2R}{c} + \alpha\mu, \quad (9)$$

where  $R = c\tau/2$  is the true radar-to-target distance. Accordingly, as depicted in Fig. 2, in the presence of an uncompensated internal delay in the radar electronics, application of the mapping rule in (7), which allows *jumping* from the domain of the measured beat frequency to the domain of the radar-to-target distances, leads to the following expression of the measured radar-to-target distance, say  $\tilde{R}$ :

$$\tilde{R} = \frac{c\tilde{f}}{2\alpha} = \frac{c\tau}{2} + \frac{c\mu}{2} = R + \frac{c\mu}{2} \quad (10)$$

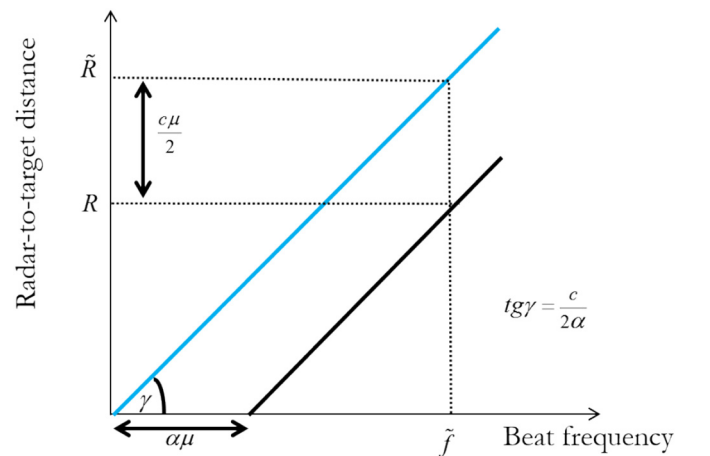
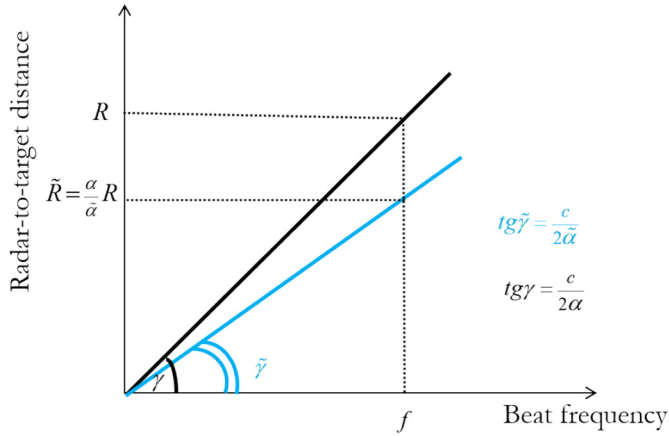


Fig. 2. Relevant to the FMCW SAR range focusing step: effect of an uncompensated propagation time delay  $\mu$  in the frequency-to-range mapping rule.  $R$  is the true radar-to-target distance.  $\tilde{R}$  is the measured radar-to-target distance. The blue line represents the used mapping rule. The black line represents the mapping rule that would lead to the true radar-to-target distance. (For interpretation of the references to colour in this figure legend, the reader is referred to the web version of this article.)



**Fig. 3.** Relevant to the FMCW SAR range focusing step: effect of a wrong knowledge of the frequency sweep rate  $\tilde{\alpha}$  in the frequency-to-range mapping rule.  $R$  is the true radar-to-target distance.  $\tilde{R}$  is the measured radar-to-target distance. The blue line represents the used mapping rule. The black line represents the mapping rule that would lead to the true radar-to-target distance. (For interpretation of the references to colour in this figure legend, the reader is referred to the web version of this article.)

which turns out to be augmented (or reduced) with respect to the true one ( $R$ ) by the term  $c\mu/2$ . This artifact represents the uncompensated time propagation delay, converted in distances, which affects the radar electronics. Note in particular that this corrupting term is unknown: it cannot be thus accounted for during the range focusing step if not properly estimated.

Let us now suppose that all the internal propagation delays present in the radar electronics are accurately known and compensated, that is,  $\mu = 0$  in (8), but the value of the frequency sweep rate (say  $\tilde{\alpha}$ ) used during the range focusing step differs from the value  $\alpha$  actually employed by the radar. More specifically, let us thus suppose that:

$$\tilde{\alpha} = \alpha + \varepsilon, \quad (11)$$

where the error  $\varepsilon$  in (11) is assumed to be constant and unknown. As depicted in Fig. 3, exploitation of the wrong frequency sweep rate in (11) during the range focusing step leads to the following mapping rule:

$$\tilde{R} = \frac{cf}{2\tilde{\alpha}} = \frac{\alpha}{\tilde{\alpha}} \frac{c\tau}{2} = \frac{\alpha}{\tilde{\alpha}} R \quad (12)$$

which produces a scaling of the measured radar-to-antenna distance (say  $\tilde{R}$ ) with respect to the true one ( $R = c\tau/2$ ). It stressed that, like the corrupting delay term  $\mu$  in (10), also the scaling term  $\alpha/\tilde{\alpha}$  in (12) is unknown; hence, it cannot be accounted for during the range focusing step if not properly estimated.

More generally, the mapping rule used during the range focusing step when both the error sources described above are present (i.e., when  $\mu \neq 0$  and  $\varepsilon \neq 0$  in (8) and (11), respectively) is easily derived from the mapping rule of Eq. (12), by substituting the expression of the beat frequency  $f$  with that found in Eq. (9). By doing so, we obtain:

$$\tilde{R} = \frac{c\tilde{f}}{2\tilde{\alpha}} = \frac{\alpha}{\tilde{\alpha}} \left( R + \frac{c\mu}{2} \right) \quad (13)$$

where  $\tilde{f}$  and  $\tilde{\alpha}$  are defined in (9) and (11), respectively. It is noted that use of the mapping in (13) leads to the calculation of a radar-to-target distance ( $\tilde{R}$ ) different from the actual one ( $R$ ). In particular, the radar-to-target distance obtained in the focused SAR image is augmented (or reduced) by a term equal to  $c\mu/2$ , and scaled by a factor equal to  $\alpha/\tilde{\alpha}$ . In other words, the unknown propagation delays occurring in the radar electronics as well as the use of a wrong frequency sweep rate during the range focusing step induce in the final focused SAR image a shift (along the range direction) of the targets' locations. The expression of this range shift, say  $\Delta R$ , can be straightforwardly derived from (13):

$$\Delta R \triangleq R - \tilde{R} = R\eta - \nu \quad (14)$$

where

$$\eta \triangleq \frac{\varepsilon}{\tilde{\alpha}}, \quad (15)$$

and

$$\nu \triangleq \frac{c\mu}{2} \frac{\alpha}{\tilde{\alpha}} = \frac{c\mu}{2} (1 - \eta). \quad (16)$$

Eq. (14) shows that the difference  $\Delta R$  between the true radar-to-target distance and that obtained in the focused SAR image can be separated into two contributions. One contribution ( $\nu$ ) is independent of the antenna-to-target distance; accordingly, it produces a rigid shift of the final focused SAR image along the range direction. The other contribution ( $R\eta$ ) depends on the (true) antenna-to-target distance. It thus produces a distortion, in particular a stretch along the range direction, of the final SAR image.

In order to compensate for these two effects, a proper estimation procedure is needed. In the next section, we propose a solution based on the joint exploitation of the SAR image affected by the above mentioned distortion effects, and in-situ measurements of a limited number of ground control points properly deployed over the area illuminated by the radar.

### 3. Proposed algorithm

The problem at hand consists in estimating the unknown electrical parameters  $\mu$  in (8) and  $\varepsilon$  in (11) or, equivalently, their counterparts  $\eta$  in (15) and  $\nu$  in (16). To do this, we exploit on one side the SAR image focused by using the frequency sweep rate provided by the radar supplier. This image is thus affected, at least in principle, by the two geometrical distortion effects discussed in Section 2. On the other side, we exploit in-situ measurements carried out on a limited number of CRs properly deployed, before the radar acquisition, over the area that will be illuminated. In particular, we exploit very precise measurements, carried out through accurate D-GPS techniques, of the positions of the phase centers of such CRs.

To estimate the unknowns  $\mu$  and  $\varepsilon$ , the information provided by the focused SAR image and the in-situ measurements carried out on the CRs are combined as follows.

On one side, we pick up from the focused SAR image the bright pixels relevant to the CRs, and calculate their range positions within the image. In other words, we find within the SAR image the peaks of the point spread functions (Franceschetti and Lanari, 1999) relevant to the CRs. In this way, for each CR we calculate the distance  $\tilde{R}$  in (13), that is, the radar-to-target distance measured by the radar. It is worth underlining that this distance, which may be affected, at least in principle, by the two artifacts in (13), can be measured in any case with an accuracy limited by the range resolution of the FMCW SAR systems. Depending on the carrier frequency, for the aerial FMCW SAR systems available in the literature (Esposito et al., 2018b; Johannes et al., 2014; Liu and Deng, 2012; Lort et al., 2018; Meta et al., 2012) this resolution can be on the order of some meters up to fraction of meter.

On the other side, starting from the D-GPS measurements of the positions of the CRs, and exploiting the accurate navigation data provided by the navigation unit mounted onboard the aerial platform that carries the radar system, we obtain for each CR an external measurement (that is, other than that achieved with the radar) of the radar-to-target distance. In this regard, we note that the accuracy of these external measurements depends on different factors. First, it depends on the accuracy of the available navigation unit. For the modern systems embedding GPS receivers and inertial navigation units, the positioning accuracy is on the order of few centimeters when proper post-processing procedures aimed at integrating D-GPS measurements and inertial data are applied (Applanix official website). Second, it depends on the accuracy of the measurement of the absolute positions of the phase

centers of the radar antennas. This procedure is typically performed in proper laboratories, such as anechoic chambers (Esposito et al., 2018a), and allows reaching accuracies on the order of fractions of wavelength, that is, centimeters or even millimeters. Third, it depends on the accuracy of the measurement of the so called lever arms, that is, the relative positions of the phase centers of the radar antennas (when they are mounted onboard the platform) with respect to the reference center of the navigation unit. This procedure is typically carried out before the airborne missions with a Total Station Theodolite (TST), which usually allows reaching accuracies on the order of millimeters. Finally, it depends on the accuracy of the in-situ measurements carried out on the CRs. The accuracy guaranteed by the D-GPS based techniques is on the order of centimeters, or even better. Overall, the accuracy of the radar-to-target distances obtained exploiting the navigation data and the in-situ measurements of the CRs' positions is on the order of centimeters, that is, not worse (typically better) than the range resolution. Hence, for each CR, these distances can be safely assumed to be the true radar-to-target distances, since they are known with an accuracy equal to (actually, higher than) the highest accuracy achievable from the SAR images, but do not contain the two artifacts in (13).

Summing up, assuming that a number  $M$  of CRs is used for our scopes, for these CRs we obtain a set  $\mathbf{R} = [R_1, R_2, \dots, R_n, \dots, R_M]^T$  of radar-to-target distances by exploiting the in-situ measurements and the navigation data, and a set  $\tilde{\mathbf{R}} = [\tilde{R}_1, \tilde{R}_2, \dots, \tilde{R}_n, \dots, \tilde{R}_M]^T$  of radar-to-target distances by exploiting the SAR image. Note that the superscripts "T" denotes the transpose operator. It is underlined that the vector  $\mathbf{R}$  contains the true radar-to-target distances, whereas the vector  $\tilde{\mathbf{R}}$  contains the radar-to-target distances affected, at least in principle, by the two artifacts in (13). Let us now rewrite the expression in (14) in a more manageable vector form:

$$\Delta\mathbf{R} = \mathbf{R}\eta - \mathbf{1}\nu \quad (17)$$

where,  $\mathbf{1} = [1, \dots, 1]^T$ , whereas  $\Delta\mathbf{R} \triangleq \mathbf{R} - \tilde{\mathbf{R}}$ . The system in (17) is linear in the unknowns  $\eta$  and  $\nu$ ; accordingly, to invert it at least two observables are necessary, that is, exploitation of at least two CRs is needed. However, to increase the robustness of the inversion, exploitation of  $M$  CRs with  $M > 2$  is more appropriate. By doing so, the system in (17) becomes overdetermined, and the two unknowns  $\eta$  and  $\nu$  can be easily estimated by addressing the following optimization problem:

$$(\hat{\eta}, \hat{\nu}) = \arg \min \text{dist}(\mathbf{R}\zeta_1 - \mathbf{1}\zeta_2, \Delta\mathbf{R}) (\zeta_1, \zeta_2) \in \mathbb{R}^2 \quad (18)$$

where the symbol " $\hat{\cdot}$ " stands for the estimate of  $a$ , and the operator  $\text{dist}(\cdot, \cdot)$  calculates the properly defined distance between the vectors. By considering for the operator  $\text{dist}(\cdot, \cdot)$  the Euclidean distance, the optimization in (18) can be solved via a LS approach (Kay, 1993), which leads to:

$$\begin{bmatrix} \hat{\eta} \\ \hat{\nu} \end{bmatrix} = (\mathbf{H}^T \mathbf{H})^{-1} \mathbf{H}^T \Delta\mathbf{R} \quad (19)$$

where  $\mathbf{H} = [\mathbf{R} \ \mathbf{1}]$  is the  $M \times 2$  model matrix.

Summing up, from the estimates in (19) we straightforwardly obtain the unknown electrical parameters  $\mu$  in (8) (through the relation in (16)) and  $\varepsilon$  in (11) (through the relations in (15) and (11)). In particular, once the parameter  $\varepsilon$  is estimated, the frequency sweep rate can be corrected and a new focusing procedure must be carried out.

Some considerations are finally in order.

First, the proposed algorithm allows estimating two unknown electrical parameters of the radar, which are supposed to be stable over the time. Thus, for a generic FMCW system the overall procedure must be applied once: the obtained estimates can be indeed used for all the other acquisition campaigns and missions carried out with the system at hand. In this regard, we stress that the estimated residual frequency sweep rate is used at the data processing level, whereas the estimated propagation delay  $\mu$  affecting the radar electronics is usually accounted

for at the hardware level directly by the radar manufacturer.

Second, it is stressed that the proposed algorithm requires to execute the overall SAR focusing procedure at least twice: first, by using the available frequency sweep rate value provided by the radar supplier; after, by accounting for the frequency sweep rate value corrected according to the estimates achieved through the inversion in (19). Possible iterations of the algorithm aimed at further refining the achieved estimates obviously involve additional executions of the focusing procedure. In this regard, it must be noted that only the illuminated areas containing the CRs must be focused to implement the proposed estimation procedure. This consideration somehow drives the strategy to be adopted for the deployment of the CRs during the campaign. Locating the different CRs approximately at the same azimuth coordinate ensures that the CRs are all imaged within a short portion of the final focused SAR image. This allows to quickly obtain the SAR image relevant to all the CRs by simply selecting a short azimuth portion of the SAR raw data, and focusing it within a range span that includes all the radar-to-CR distances. In this regard, we also note that the estimation error involved in (19) is given by the projection of the noise that unavoidably affects the observable  $\Delta\mathbf{R}$  onto the subspace spanned by the columns of the model matrix  $\mathbf{H}$ , see (Kay, 1993). It can be easily shown (Kay, 1993) that such a projection is inversely proportional to the determinant of the matrix  $\mathbf{H}^T \mathbf{H}$ , which in our case is given by:

$$\det(\mathbf{H}^T \mathbf{H}) = M^2 \left[ \frac{1}{M} \sum_{m=1}^M R_m^2 - \left( \frac{1}{M} \sum_{m=1}^M R_m \right)^2 \right] \quad (20)$$

and it is thus proportional to the variance of the vector  $\mathbf{R}$ , being  $M^2$  the corresponding proportionality constant. This implies first of all that (not surprisingly) the higher the number  $M$  of deployed CRs, the less the estimation error involved in (19). More important, the higher the variance of the elements of the vector  $\mathbf{R}$ , the less the estimation error involved in (19). This means that to improve the performances of the proposed algorithm, the CRs positions must be well spread along the range swath covered by the radar antenna. Accordingly, by referring to the two geometric coordinates of the SAR images, to speed up the overall proposed procedure, the CRs must be deployed within an azimuth strip as narrow as possible, whereas to improve the accuracy of the proposed procedure, they must be deployed within a range portion as wide as possible.

#### 4. Results

The presented algorithm has been tested on real data acquired by the Italian AXIS system (Esposito et al., 2018b), which is a single-pass interferometric airborne X-band FMCW SAR manufactured by Elettra Microwave. In particular, the results reported in this section are relevant to a dataset acquired during an airborne campaign carried out in 2018 over the city of Salerno, South of Italy. For this campaign, the system was installed onboard a Cessna 172 airplane. The main mission, system and focusing parameters are listed in Table I. More details can be found in (Esposito et al., 2018b).

During the campaign, five CRs were deployed within the

**Table I**  
Main mission, system and focusing parameters.

Mean aircraft altitude	2500 m
Mean aircraft velocity	48 m/s
Slant range swath	5.67 km
Central frequency	9.55 GHz
Bandwidth	200 MHz
Chirp duration	600.184 $\mu$ s
PRF	1200 Hz
Sampling frequency	25 MHz
Azimuth resolution	0.35 m
Range resolution	0.75 m

illuminated area (specifically, over the airport runway) and very accurate DGPS measurements of their positions were carried out. These in-situ measurements along with the navigation data recorded onboard the airplane during the acquisition flight, allowed us to calculate the radar-to-target distances relevant to the considered CRs. In this regard, it is stressed that the AXIS system embeds a modern navigation unit, namely, the Applanix POS-AV 510, which provides very accurate information of the flight paths ([Applanix official website](#)). Moreover, the absolute position of the phase centers of the radar antennas has been measured very accurately in anechoic chamber ([Esposito et al., 2018a](#)) before the airborne campaign. Finally, during the mission, once the system was installed onboard the airplane, the lever arms were measured very precisely by means of a TST. According to all these adopted practices, we can safely assume that the radar-to-target distances relevant to the CRs and obtained through the in-situ measurements of their positions and the flight data provided by the navigation unit, are known with an accuracy of few centimeters, which is a value much finer than the range resolution of the radar system (see [Table I](#)). These distances can be thus assumed to be the true radar-to-target distances relevant to the five considered CRs.

According to the considerations done in the previous section, we have deployed the CRs along a short azimuth portion ( $< 500$  m) of the overall area (whose azimuth extension is about 20 km) that we planned to illuminate with the radar. To apply our procedure, we have thus focused only a short portion of the entire acquired data-set. The range focusing step has been carried out by exploiting the frequency sweep rate value provided by the radar supplier, namely,  $\bar{\alpha} = 3.30371e11 \text{ s}^{-2}$ . Following the range focusing step, a time-domain back projection strategy ([Soumekh, 1999](#)) has been applied to focus the data also along the azimuth direction ([Franceschetti and Lanari, 1999](#)). As specified above, the main focusing parameters are listed in [Table I](#).

[Fig. 4](#) shows the (multi-look) amplitude SAR image, represented in radar grid (that is, in range-azimuth coordinates), of the illuminated area. The five CRs are highlighted with red circles. The CRs are confined in a range span of about 700 m: in particular, the radar-to-target distances relevant to the nearest and farthest CRs are about 3.1 km and 3.8 km, respectively.

To roughly evaluate if the focused SAR image of [Fig. 4](#) is affected by the geometric artifacts described in [Section 2](#), in [Fig. 5\(a\)](#) we represent it in geographic grid over a Google Earth orthophoto. [Fig. 5\(b\)](#) shows the sole Google Earth orthophoto, whereas [Fig. 5\(c\)](#) shows a semi-transparent overlay of the SAR image on the Google Earth orthophoto. Note that in [Figs. 5\(a\)](#) and (b) we have also represented in geographic grid the (mean) axes of the radar grid. In the selected area, we have identified three features clearly observable in both the SAR image (green arrows) and the orthophoto (red arrows). [Fig. 5\(c\)](#) clearly shows that the SAR image is shifted along the range direction with respect to the orthophoto, which can be considered, at least at first sight, the truth.

To compensate such effects, we have applied the estimation procedure described in [Section 3](#), by exploiting the true radar-to-target distances calculated for the five considered CRs. To this aim, we have built the vector  $\Delta \mathbf{R}$  and the model matrix  $\mathbf{H}$  in (19). In [Fig. 6](#) we plot (red dots) the values of the elements of  $\Delta \mathbf{R}$  (which are reported also in [Table II](#), first column) as a function of those of  $\mathbf{R}$ . The plot shows that the range location errors occurring in the focused SAR image and measured in correspondence of the five CRs (that is, the values of  $\Delta \mathbf{R}$ ) are on the order of 30 m. Moreover, the plot clearly shows that these errors are not constant and depend almost linearly on the corresponding radar-to-target distances (that is, the values of  $\mathbf{R}$ ). To highlight this behavior, in [Fig. 6](#), we plot also the linear fitting (black line) of the reported measurement results. According to [Eq. \(14\)](#), this linear trend is mainly due to the use of an erroneous frequency sweep rate during the range focusing step.

Application of the optimization procedure in (19) has led to the estimates reported in the first column of [Table III](#). By inserting in (11)



**Fig. 4.** Multi-look amplitude SAR image of a  $0.55 \text{ km} \times 2.8 \text{ km}$  wide patch of the entire acquired strip. Spatial resolution:  $1.5 \text{ m (range)} \times 1.25 \text{ m (azimuth)}$ . Red circles indicate the CRs' positions. (For interpretation of the references to colour in this figure legend, the reader is referred to the web version of this article.)

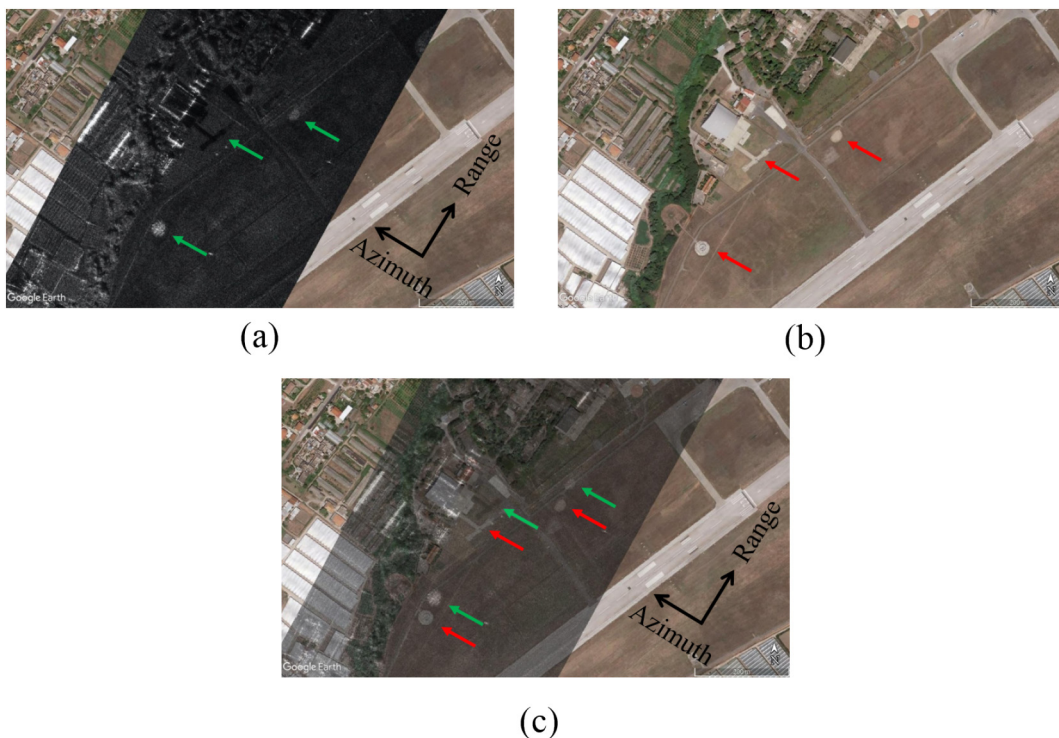


Fig. 5. (a) Amplitude SAR image (in geographic grid) obtained by exploiting during the focusing step the frequency sweep rate provided by the radar supplier. (b) Google Earth orthophoto relevant to the same area. (c) A semi-transparent overlay of the image in (a) on the orthophoto in (b). The green and red arrows indicate the positions of three features clearly visible in both the SAR image and the orthophoto. (For interpretation of the references to colour in this figure legend, the reader is referred to the web version of this article.)

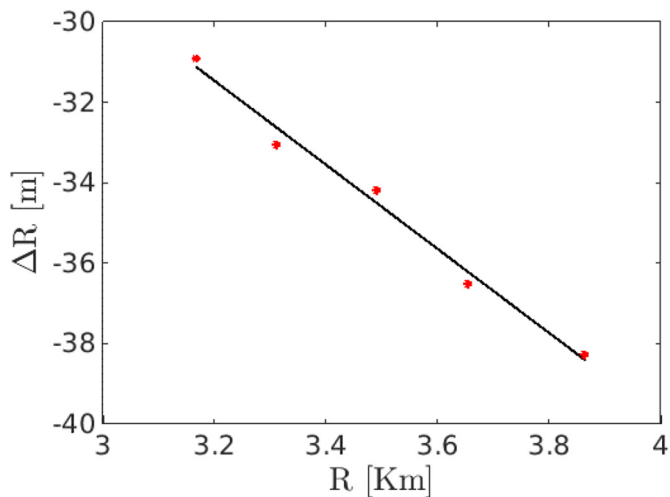


Fig. 6. Range Difference Vector as a function of the range vector.

Table II  
Range location errors occurring in the focused SAR image and measured in correspondence of the five CRs.

	Focused image 1 $\tilde{\alpha} = 3.30371e11 \text{ s}^{-2}$	Focused image 2 $\tilde{\alpha} = 3.33788e11 \text{ s}^{-2}$	Focused image 3 $\tilde{\alpha} = 3.33598e11 \text{ s}^{-2}$
	$\Delta R$	$\Delta R_s$	$\Delta R_t$
CR1	-30.88 m	2.0 m	0.21 m
CR2	-33.03 m	2.15 m	0.27 m
CR3	-34.17 m	2.24 m	0.26 m
CR4	-36.50 m	2.50 m	0.42 m
CR5	-38.25 m	2.34 m	0.15 m

Table III  
Results of the estimates obtained through the proposed algorithm.

	Focused image 1 $\tilde{\alpha} = 3.30371e11 \text{ s}^{-2}$	Focused image 2 $\tilde{\alpha} = 3.33788e11 \text{ s}^{-2}$	Focused image 3 $\tilde{\alpha} = 3.33598e11 \text{ s}^{-2}$
$\hat{\eta}$	$-1.03e-2$	$5.67e-4$	$-2.95e-7$
$\hat{\nu}$	1.95 m	0.26 m	0.26 m
$\hat{\epsilon}$	$-3.41e9 \text{ s}^{-2}$	$1.89e8 \text{ s}^{-2}$	$-9.87e4 \text{ s}^{-2}$
$\hat{\mu}$	$1.28e-8 \text{ s}$	$1.78e-9 \text{ s}$	$1.78e-9 \text{ s}$

the estimated value  $\hat{\epsilon}$ , we corrected the frequency sweep rate provided by the radar supplier, obtaining  $\tilde{\alpha} = 3.33788e11 \text{ s}^{-2}$  (as reported in Tables II and III, second column). Then, we executed once again the overall SAR focusing procedure (including the range focusing step) by exploiting this refined value of  $\tilde{\alpha}$ . In this way, we have generated a new focused image, say image 2. Starting from the information coming from this image and exploiting the in-situ measurements, we built again the vector of the range errors in (19). The values of the elements of this vector, say  $\Delta R_s$ , are reported again in Table II (second column). As can be seen, a residual range location error (on the order of 2 m) is still measured in correspondence of the CRs. Moreover, a linear trend of this error with respect to the radar-to-target distances seems to be still present. The presence of these residual artifacts is maybe due to the higher order effects that are not accounted for by the proposed model and that affect the overall focusing procedure that follows the range focusing step (Fornaro et al., 2005). To further refine the obtained estimates, we carried out an additional iteration of the algorithm, that is, we applied again the optimization procedure in (19), by exploiting the updated vector  $\Delta R_s$  (note that the model matrix  $\mathbf{H}$  is the same as that used in the previous iteration of the algorithm). By doing so, we obtained the estimates reported in the second column of Table III. In this regard, we note that from the estimated value  $\hat{\eta}$  it turns out that in the image 2 the location error of the far range targets is on the order of

about 3 m (see Eq. (14) and consider that the for the considered radar acquisition the far range is equal to 5670 m). A further refinement of the frequency sweep rate to be used during the focusing procedure is thus still needed. Accordingly, by using the estimates reported in the second column of Table III, we have further corrected the frequency sweep rate, by obtaining  $\tilde{\alpha} = 3.33598e11 \text{ s}^{-2}$ . Then, we executed once again the overall SAR focusing procedure with this refined value of  $\tilde{\alpha}$ . In this way, we generated a new focused image, say image 3. Starting from the information coming from this image and exploiting the in-situ measurements we built again the vector of the range errors in (19). The values of the elements of this vector, say  $\Delta R_r$  are reported again in Table II (third column). As can be seen, a very residual range location error, ranging from 15 cm to 45 cm, is now present in correspondence of the CRs. It is worth underlining that this error is smaller than the range resolution of the system (see Table I). Accordingly, it has no sense to pursue further reduction of this residual range shift still present in the image. To show this, we applied again the optimization procedure in (19) by exploiting the updated vector  $\Delta R_r$ . By doing so, we obtained the estimates reported in the third column of Table III, from which we understand that the main contribution to the residual range location errors measured in the image 3 in correspondence of the CRs is systematic ( $\hat{v} = 26 \text{ cm}$ ). Moreover, by using in Eq. (14) the estimated value  $\hat{\eta}$ , it turns out that in the image 3 the range-dependent contribution of the location error (namely,  $\hat{\eta}R$ , see (14)) is in the worst case (that is, for the far range targets) on the order of few millimeters. The frequency sweep rate exploited during the focusing procedure to generate the image 3 is thus the ending value that we were searching. In this regard, we observe that by carrying out further iterations of the overall algorithm (which involves the application of the optimization in (19) followed by a complete SAR data focusing procedure) we have always obtained (results are not reported for brevity) practically the same estimates reported in the third column of Table III.

To appreciate the effectiveness of the applied procedure, in Fig. 7 we show the same analysis as that in Fig. 5, by replacing the focused image 1 with the focused image 3. As can be seen, the range shift of the

overall SAR image, clearly visible in Fig. 5(c), disappears in Fig. 7(c).

## 5. Conclusions

This paper addresses the distortion effects observable in FMCW SAR images and due to the use, during the data focusing step, of a frequency sweep rate value different from that actually employed by the radar. In particular, we have proposed an algorithm that obtains an accurate and fast estimate of the actual radar frequency sweep rate, thus providing a key information that can be then profitably used to achieve the correct focusing of the SAR data acquired by the radar system at hand.

The presented approach makes use of in-situ measurements of the positions of a limited number of CRs properly deployed over the observed scene. In particular, it is based on a LS approach that provides, in addition to the estimate of the searched frequency sweep rate, also the estimate of the internal uncompensated time delay that may be present in the radar electronics.

The presented algorithm requires to execute the overall SAR focusing procedure at least twice: first, by using the available frequency sweep rate value provided by the radar supplier, after, by accounting for the achieved estimates. Additional iterations of the algorithm may be in principle needed to further refine the obtained estimates. However, at least for the considered data sets, just few iterations of the procedure are sufficient to achieve a sound estimate of the desired frequency sweep rate.

The algorithm has been tested on a real X-band dataset acquired in 2018 by an X-Band airborne FMCW SAR system. To apply the proposed approach, we have deployed five CRs over the illuminated scene. For this considered data set, the SAR image focused with the frequency sweep rate provided by the radar supplier turned out to be severely stretched in the range direction. In particular, from the surveys on CRs we measured a misalignment on the order of 30 m between the actual CRs' positions and those calculated in the focused image. Two iterations of the proposed algorithm have led to a focused image in which this misalignment has been reduced to a mean value of 26 cm, that is, much

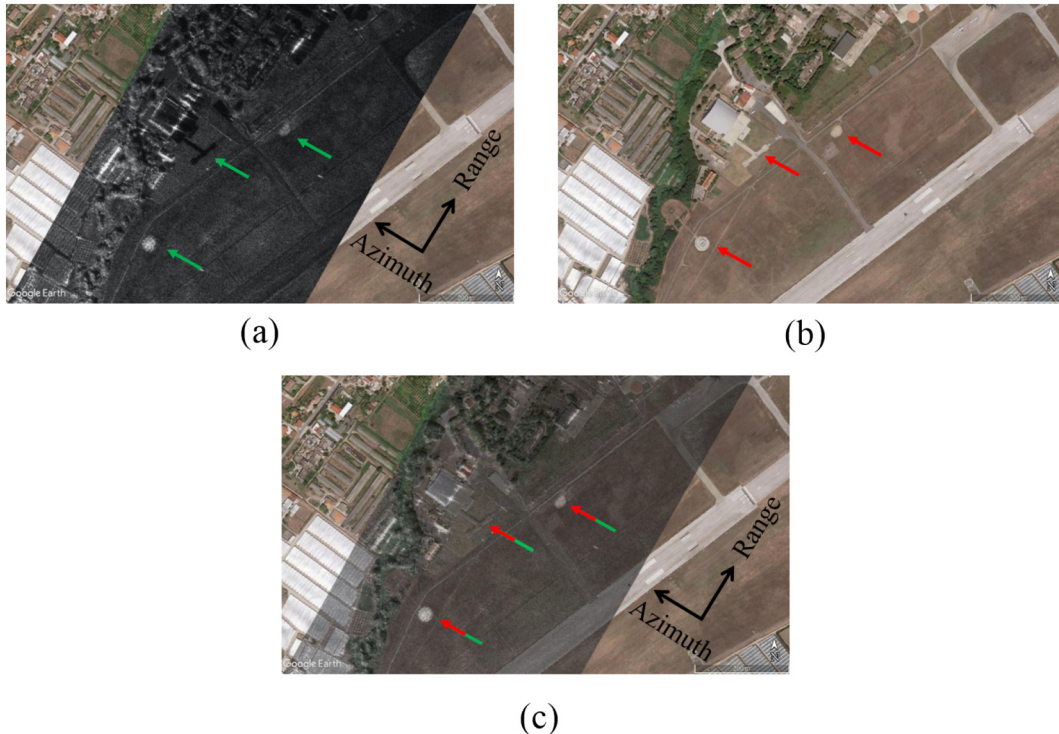


Fig. 7. (a) As Fig. 5, but for the SAR image, which in this case has been focused by exploiting the frequency sweep rate different from that provided by the radar supplier, and calculated through the proposed algorithm.

smaller than the range resolution of the system, thus assessing the effectiveness of the overall presented approach. We, finally, stress that the proposed approach has been tested on an airborne SAR system; notwithstanding, it also can be used for rail-SAR or other near range SAR applications.

## Acknowledgments

This work has been supported in part by the Italian Department of Civil Protection (DPC) in the framework of DPC-IREA Agreement (2019-2021) and in part by the Italian Ministry of Economic Development (MISE) in the framework of the contract "MATRAKA".

The authors would like to thank Dr. A. Pauciuolo of IREA- CNR for the useful discussions.

## References

- Aguasca, A., Acevo-Herrera, R., Broquetas, A., Mallorqui, J.J., Fabregas, X., 2013. ARBRES: light-weight CW/FM SAR sensors for small UAVs. *Sensors* 13, 3204–3216. [Applanix official website](http://www.applanix.com) <http://www.applanix.com>.
- Buckreus, S., Werninghaus, R., Pitz, W., 2009. The German satellite mission TerraSAR-X. *Aerosp. Electron. Syst.* 24 (11).
- De Zan, F., Monti Guarnieri, A., 2006. TOPSAR: terrain observation by progressive scans. *IEEE Trans. Geosci. Remote Sens.* 44 (9), 2352–2360.
- Esposito, C., Gifuni, A., Perna, S., 2018a. Measurement of the antenna phase center position in anechoic chamber. *IEEE Antennas Wirel. Propag. Lett.* 17 (12), 2183–2187.
- Esposito, C., Natale, A., Berardino, P., Palmese, G., Lanari, R., Perna, S., 2018b. AXIS: An airborne X-band interferometric FMCW SAR system. In: *Proceedings of the IEEE International Geoscience and Remote Sensing Symposium, Valencia*, pp. 5697–5699.
- Fornaro, G., Franceschetti, G., Perna, S., 2005. Motion compensation errors: effects on the accuracy of airborne SAR images. *IEEE Trans. Aerosp. Electron. Syst.* 41 (4), 1338–1352.
- Franceschetti, G., Lanari, R., 1999. *Synthetic Aperture Radar Processing*. CRC Press, New York, NY, USA.
- Gebert, N., Krieger, G., Moreira, A., 2010. Multichannel azimuth processing in ScanSAR and TOPS mode operation. *IEEE Trans. Geosci. Remote Sens.* 48 (7), 2994–3008.
- Hensley, S., Chapin, E., Freedman, A., Le, C., Madsen, S., Michel, T., Rodriguez, E., Siqueira, P., Wheeler, K., 2001. First P-band results using the Geosar mapping system. In: *Proceedings of the IEEE International Geoscience and Remote Sensing Symposium, Sydney, Australia*, pp. 126–128.
- Horn, R., Nottensteiner, A., Reigber, A., Fischer, J., Scheiber, R., 2009. F-SAR—DLR's new multifrequency polarimetric airborne SAR. In: *Proceedings of the IEEE International Geoscience and Remote Sensing Symposium, Cape Town, South Africa*, pp. 902–905.
- IEEE Standard Definitions of Terms for Antennas, 1983. *IEEE Standard* 145. pp. 1–31.
- Johannes, W., et al., 2014. Implementation of a 35 GHz SAR sensor and a high resolution camera to enable real-time observation. In: *Proceedings of the European Conference on Synthetic Aperture Radar, Berlin, Germany*, pp. 1–4.
- Kay, S.M., 1993. *Fundamentals of Statistical Signal Processing—Estimation Theory*. Prentice-Hall, Englewood Cliffs, NJ, USA.
- Liu, Y., Deng, Y., 2012. CARMSAR—a compact and reconfigurable miniature SAR system for high resolution remote sensing. In: *Proceedings of the European Conference on Synthetic Aperture Radar, Nuremberg, Germany*, pp. 294–297.
- Lort, M., Aguasca, A., López-Martínez, C., Marín, T.M., 2018. Initial evaluation of SAR capabilities in UAV multicopter platforms. *Proc. IEEE J. Sel. Top. Appl. Earth Obs. Remote Sens.* 11 (1), 127–140.
- Meta, A., Hoogeboom, P., Ligthart, L.P., 2007. Signal processing for FMCW SAR. *IEEE Trans. Geosci. Remote Sens.* 45 (11), 3519–3532.
- Meta, A., Imbembo, E., Trampuz, C., Coccia, A., De Luca, G., 2012. A selection of MetaSensing airborne campaigns at L, X- and kuband. In: *Proceedings of the European Conference on Synthetic Aperture Radar, Nuremberg, Germany*, pp. 414–417.
- Moreira, A., Prats-Iraola, P., Younis, M., Krieger, G., Hajnsek, I., Papathanassiou, K.P., 2013. A tutorial on synthetic aperture radar. *IEEE Geosci. Remote Sens. Mag.* 1 (1), 6–43.
- Perna, S., Esposito, C., Amaral, T., Berardino, P., Jackson, G., Moreira, J., Pauciuolo, A., Vaz Junior, E., Wimmer, C., Lanari, R., 2016. The InSAeS4 airborne X-band interferometric SAR system: a first assessment on its imaging and topographic mapping capabilities. *Remote Sens.* 8, 40.
- Perna, S., et al., 2019. The Asi P-Band Helicopter-Borne Integrated Sounder-Sar System: Preliminary Results of the 2018 Morocco Desert Campaign. (accepted for publication in the *Proceedings of IEEE International Geoscience and Remote Sensing Symposium, Japan*).
- Pinheiro, M., Reigber, A., Scheiber, R., Prats-Iraola, P., Moreira, A., 2018. Generation of highly accurate DEMs over flat areas by means of dual-frequency and dual-baseline airborne SAR interferometry. *IEEE Trans. Geosci. Remote Sens.* 56 (8), 4361–4390.
- Richards, M.A., Scheer, J.A., Holm, W.A., 2010. *Principles of Modern Radar: Basic Principles*. SciTech Publishing, Raleigh, NC, USA.
- Rombach, M., Fernandes, A.C., Luebeck, D., Moreira, J., 2003. Newest technology of mapping by using airborne interferometric synthetic aperture radar systems. In: *Proceedings of the IEEE International Geoscience and Remote Sensing Symposium*.
- Ruault du Plessis, O., Nouvel, J., Baque, R., Bonin, G., Dreuillet, P., Coulombaix, C., Oriot, H., 2011. ONERA SAR facilities. *IEEE Aerosp. Electron. Syst. Mag.* 26, 24–30.
- Soumekh, M., 1999. *Synthetic Aperture Radar Signal Processing: With MATLAB Algorithms*. Wiley, Hoboken, NJ.
- Tarchi, D., Casagli, N., Fanti, R., Leva, D.D., Luzi, G., Pasuto, A., Pieraccini, M., Silvano, S., 2003. Landslide monitoring by using ground-based SAR interferometry: an example of application to the Tessina landslide in Italy. *Eng. Geol.* 68 (1–2), 15–30.
- Teichman, M., 1973. Determination of horn antenna phase centers by edge diffraction theory. *IEEE Trans. Aerosp. Electron. Syst.* 9 (6), 875–882.
- Tomiyasu, K., 1981. Conceptual performance of a satellite borne, wide swath synthetic aperture radar. *IEEE Trans. Geosci. Remote Sens.* 2, 108–116.
- Torres, et al., 2012. GMES Sentinel-1 mission. In: *Special Issue of Journal of Remote Sensing of Environment "The Sentinel Missions: New Opportunities for Science"*. vol. 120. pp. 9–24.
- Venturini, R., et al., 2008. Experimental verification of COSMOSkyMed SAR capabilities. In: *Proceedings of the IEEE Radar Conference, Rome*, pp. 1–5.
- Wimmer, C., Siegmund, R., Schwabisch, M., Moreira, J., 2000. Generation of high precision DEMs of the Wadden Sea with airborne interferometric SAR. *IEEE Trans. Geosci. Remote Sens.* 38 (5), 2234–2245.